SCIENCE CHINA
Earth Sciences

•RESEARCH PAPER•

September 2020 Vol.63 No.9: 1294–1308
https://doi.org/10.1007/s11430-019-9616-y

Cenozoic magmatic activity and oblique uplifting of the Ailao Mountain: Evidence from a short-period dense seismic array

Lu ZHANG[1,2], Zhiming BAI[1,3*], Tao XU[1,4], Zhenbo WU[5], Minfu HUANG[1,2], Guiping YU[1,2], Junlei CHEN[1,2,6] & Mengjie ZHENG[1,2]

[1] *State Key Laboratory of Lithospheric Evolution, Institute of Geology and Geophysics, Chinese Academy of Sciences, Beijing 100029, China;*
[2] *University of Chinese Academy of Sciences, Beijing 100049, China;*
[3] *Innovation Academy for Earth Science, Chinese Academy of Sciences, Beijing 100029, China;*
[4] *CAS Center for Excellence in Tibetan Plateau Earth Sciences, Beijing 100101, China;*
[5] *School of Geophysics, Chengdu University of Techonology, Chengdu 610059, China;*
[6] *Earthquake Administration of Yunnan Province, Kunming 650224, China*

Received December 15, 2019; revised April 13, 2020; accepted April 20, 2020; published online May 25, 2020

Abstract Geological studies show that the southern part of Ailaoshan-Red River shear zone (ALSRRSZ) has experienced complex metallogenic processes and multi-stage non-uniform uplifting, called oblique uplifting since the Cenozoic. To detect the deep structure and geodynamic background beneath Daping, Chang'an and other gold and polymetallic deposits in this area, we carried out a high-density short-period seismic array survey in southern Yunnan province. The array used is approximately 240 km long with an interval of 500 m between two adjacent stations. Based on the data collected by the array, we used *H*-κ stacking and common conversion point (CCP) methods of receiver functions to reveal the fine crustal structure beneath this array, which was located from Lvchun (western end) to the east and ended in Maguan. The three main conclusions are as follows. (1) The average crustal thickness is approximately 37 km and the V_p/V_s ratio is 1.75. However, the thickness and V_p/V_s ratio of the Ailao Mountain are rather greater or higher than those of the western Lanping-Simao Basin and eastern South-China block. These results may indicate that the crust is rich in ferromagnesian minerals or has a thermal fluid anomaly after orogenic movement. (2) There are two obvious inclined interfaces beneath the Ailao Mountain in the mid-upper crust, which suggests that strong deformation occurred there during the orogenic period. Some evidences, such as the weak converted-wave Pms phase from the Moho, low P-wave velocities of the upper mantle, high surface heat flow values, and generally developed hot springs, indicate that a strong crust-mantle interaction exists in the southern segments of the Ailaoshan-Red River shear zone. These interactions include a diapir of mantle-sourced magma (stronger in the east than that in the west), lateral collision from the Indian Plate, and the differential uplift caused by the strike-slip movement of the Red River Fault. All of above deep processes led to the Cenozoic oblique uplifting of Ailao Mountain. (3) By combining the location of the deposits on the surface, characteristics of the average crustal V_p/V_s ratio, hypocenters of the small earthquakes along the research profile, Moho shape, and horizontal variations of the Pms phase amplitudes, we speculate that the Ailaoshan Fault was the upgoing conduit for metallogenic magma and played a significant role in the Cenozoic development of the multiform metal deposits around the Ailao Mountain area.

Keywords Ailaoshan-Red River shear zone, Multiform metal deposits, Oblique uplifting, Short-period dense seismic array, Receiver function

Citation: Zhang L, Bai Z, Xu T, Wu Z, Huang M, Yu G, Chen J, Zheng M. 2020. Cenozoic magmatic activity and oblique uplifting of the Ailao Mountain: Evidence from a short-period dense seismic array. Science China Earth Sciences, 63: 1294–1308, https://doi.org/10.1007/s11430-019-9616-y

* Corresponding author (email: bbzzmm@mail.iggcas.ac.cn)

1. Introduction

The continuous collision between the Indo-Eurasian continent since the Cenozoic era has created the "Roof of the World" Himalayan and many other active mountain systems in Asia and has activated a series of large-scale strike-slip faults. Researchers have demonstrated that the material inside the Tibetan Plateau were extruded as a rigid block in the east and southeast directions (Tapponnier and Molnar, 1977; Tapponnier et al., 1982) during the collision, which have a significant impact on the adjacent area geomorphic patterns and environmental evolution (Peltzer and Tapponnier, 1988; Avouac and Tapponnier, 1993; Xu et al., 2011). The Ailaoshan-Red River shear zone (ALSRRSZ), which is located in the Sanjiang metallogenic belt on the southeastern margin of the Tibetan Plateau, is the boundary of the Indochina block to the west and the South-China block to the east (Figure 1). It is a key location where the Indo-Eurasian plate converges laterally and the material inside the plateau is extruded southward along the Red River Fault. Therefore, this area is an ideal location for studying the geodynamic process of lateral-collision orogeny and the growth mechanisms of the plateau (Peltzer and Tapponnier, 1988; Tapponnier et al., 1990).

There are many porphyry and orogenic type gold and polymetallic deposits in the southern part of the ALSRRSZ, such as the Tongchang, Habo, Daping, and Chang'an (Figure 1). These deposits form an important part of the lateral-collision metallogenic belt whose mineralization ages range from the late Eocene to early Oligocene (34±2 Ma) (Wang et al., 2005; Tian et al., 2014) on the Tibetan Plateau. Researchers in different fields have studied the orogenic process and mechanisms of the metallogenic belt by using different approaches, such as petrology, tectonic geology, and geochemistry (Hou et al., 2004, 2017; Deng et al., 2013; Sun et al., 2018). Some important perspectives have been proposed such as the genesis of the deposit is related to the intra-crust magma and fluid effects caused by post-collision extension and intracontinental orogenic transformation and the large-scale alkali-rich magma caused by the strong crust-mantle interaction in the Himalayas is the important source of ore-forming materials and fluid (Zhu et al., 2009; Cong et al., 2013; Tian et al., 2014).

Moreover, the evidence shows that the Diancang Mountain-Ailao Mountain area had experienced multiple magma eruption and mountain uplift events since Cenozoic (Li et al., 2001; Wang et al., 2006; Li et al., 2016). Li et al. (2012) determined that differential uplift took place in Ailao Mountain area from approximately 5 Ma and was characterized by the uplift of the east being greater than that in the west which caused the oblique uplifting pattern of Ailao Mountain. Also, the Red River Fault, which is located in the eastern side of the ALSRRSZ, has long been considered as an important boundary of the southeastern margin of the Tibetan Plateau and many studies have been conducted to explore its activity situation and deformation characteristics (Zhong and Ding, 1996; Leloup et al., 1993, 1995; Li et al., 2001; Wan et al., 2000; Wang et al., 2006). However, there are still disagreements on its activity timing and spatial distribution. For example, a question that does not yet have a consensus answer is whether the Red River Fault is a deep fault cutting through the lithosphere (Tapponnier et al., 1982, 1990; Leloup et al., 1995; Wan et al., 2000).

Above analysis indicates that remarkable magmatic activity and tectonic movement have taken place in the ALSRRSZ since the Cenozoic. However, due to the lack of deep geophysical data, it is difficult to answer such scientific questions as whether the material and magmatic hydrothermal fluids related to orogeny and mineralization are retained in the deep crust and what are the characteristics of crustal deformation and rock properties within the ALSRRSZ? Large-scale imaging studies have been conducted on crust-mantle structures to reveal the velocity variation features around ALSRRSZ and its adjacent area by employing P-wave travel time inversions (Liu et al., 2000; Xu, 2005; Zhang et al., 2018), wide-angle refraction/reflection (Bai and Wang, 2004; Wang et al., 2014; Xu T et al., 2015; Pan et al., 2015), Rayleigh wave tomography (Fu et al., 2017), and joint inversions of receiver functions and Rayleigh wave dispersion (Bao et al., 2015). However, these previous studies were based on geophysical observation of large station spacing and only have low horizontal resolution, hence they were difficult to describe the crustal structure and deformation features subtly of studied area. So far, there is still a lack of high-resolution geophysical exploration profiles across the key ore clusters in the southern part of Ailao Mountain area. Funded by the national key research and development program entitled "Deep Structures and Metallogenic Process of Collisional Orogenic Metallogenic System in Tibetan Plateau", we conducted a high-density seismic survey across ALSRRSZ in southern Yunnan province. This article reports on the results of receiver function H-κ stacking and CCP imaging. Their geodynamic significance and metallogenic implications in the Ailao Mountain area are also discussed.

2. Data and method

2.1 Date selection

The short-period, dense seismic array has a total length of approximately 240 km and starts in Lvchun county in the west and ends nears Maguan county in the east (Figure 1). It spans three tectonic units from west to east, including the Lanping-Simao Basin, Ailaoshan-Red River shear zone, and South-China block. A total of 480 seismic stations were

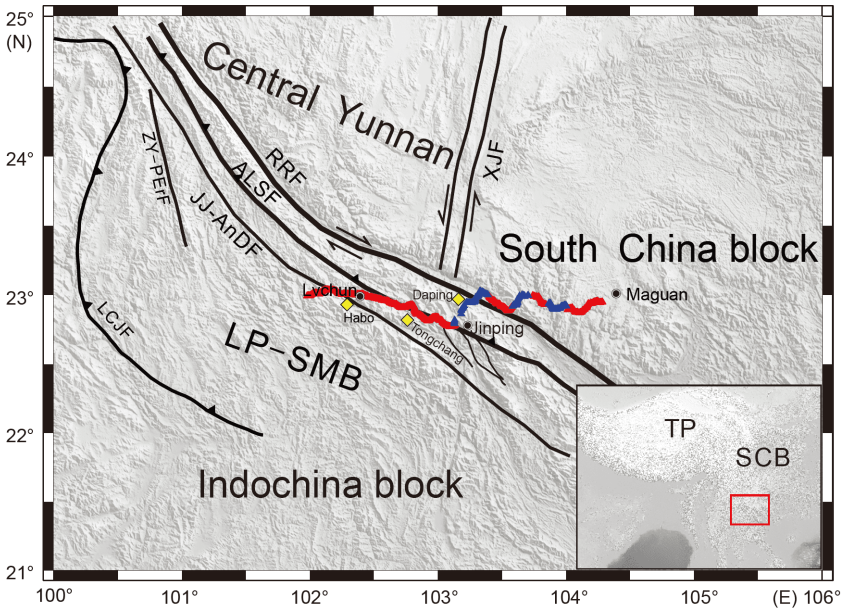

Figure 1 Topographic map of tectonic blocks, faults, and seismic station locations in the research area. LP-SMB, Lanping-Simao Basin; XJF, Xiaojiang Fault; RRF, Red River Fault; ALSF, Ailaoshan Fault; JJ-AnDF, Jiujia-Anding Fault; ZY-PErF, Zhenyuan-Pu'er Fault; LCJF, Lancangjiang Fault; Yellow diamonds, ore deposit locations; red triangles, PDS-2 instruments; blue triangles, EPS instruments. The inset shows the research area (red solid box). TP, Tibetan Plateau; SCB, Sichuan Basin.

deployed, including 362 PDS-2 and 118 EPS short-period seismic instruments at intervals of 500 m. The observation period was 35 days from December, 2017 to January, 2018. Based on the earthquake catalog (USGS-NEIC: https://earthquake.usgs.gov/earthquakes/search/), 31 earthquakes with magnitude >5.2 were collected from the original continuous data and with epicentral distances between 28° and 95° to calculate P-wave receiver functions.

2.2 Receiver-function process technique

The teleseismic P-wave receiver-function method has been broadly used for imaging the crust and upper mantle (Owens et al., 1984; Chen et al., 2005; Zheng et al., 2012; Wu et al., 2016). Its principle is that when a teleseismic P-wave is incident to a horizontal interface beneath the station and across it, the converted Ps seismic phase and its multiple waves (PpPs and PsPs+PpSs) are generated. The specific descriptions of how to use receiver functions to study structures below a station are as follows: first, the radial or tangential components are deconvolved from the vertical component and the time delays of the Ps phase and its multiples are extracted. Then, based on the back azimuth and ray parameters and also using a given velocity model, the ray paths within the medium are tracked in inverse and the receiver functions in the time domain are converted into the depth sequence to reveal the shapes of the interfaces within the crust and Moho (Langston, 1977; Xu and Zhao, 2008). Based on the continuous observation data from 480 short-period seismometers, imaging of the crust-mantle interface below the dense array was carried out. The dense distribution of stations greatly increased the sampling of the Ps phase, which effectively enhanced the coherent signals and suppressed the noise in CCP imaging. In this manner, finer crustal structures could be depicted compared to those obtained from traditional broadband observations.

First, data preprocessing was conducted and included application of demean, detrend, taper, resample, and coordinate rotation operations on the raw data. Second, all preprocessed traces were subjected to bandpass filtering between 0.05–5.0 Hz with 4th order Butterworth bandpass filter. Generally, the low frequency portions of seismic waves mainly contain large-scale structural information while the high-frequency data can reveal small-scale structures. The cutoff frequencies of the PDS-2 and EPS instruments are 0.5 and 0.2 Hz, respectively, so we expected to preserve more low frequency signals to produce stable results. Considering the narrowband characteristics of short-period instruments, we considered it necessary to enhance the amplitude of the low frequencies by removing the instrument responses. This paper uses the EPS short-period seismograph with station number is 4337 as an example (Figure 2). It shows the radial component, vertical component, and receiver function before and after removing the instrument response. The M_s6.5 event (2017.12.15.16.47.58) came from the eastern direction of the profile and its epicenter was at 108.17°E and 7.49°N. We can see that although the seismic waves and receiver functions before and after instrument response removal are quite similar, the waveforms after the response removal step contain lower-frequency information, which is helpful for providing

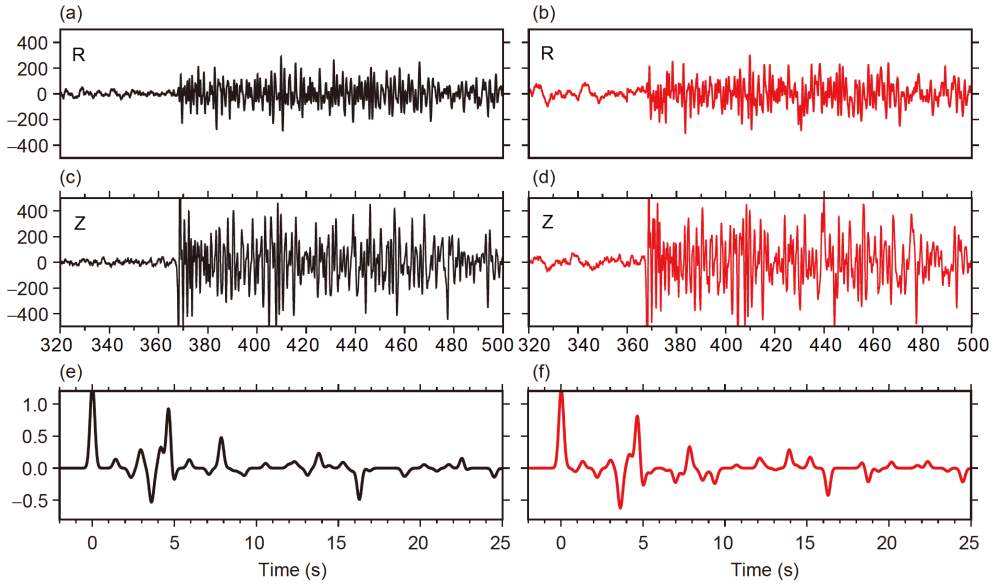

Figure 2 Comparison of the radial component, vertical component, and receiver-function waveforms from EPS short-period seismography before and after removing the instrument response. (a), (c), and (e) are the waveforms before removing the instrument response; (b), (d) and (f) are the waveforms after removing the instrument response.

more stable information to reveal the deep structures of the interfaces.

Then, all waveforms from the 31 magnitude >5.2 events were windowed to 10 s before and 40 s after the P-wave arrivals. This duration is sufficiently long to cover Ps and its multiples from the crustal interfaces and the Moho. Finally, a time domain iterative deconvolution algorithm (Ligorria and Ammon, 1999) with a Gaussian value of 5.0 was used to calculate the receiver functions. Due to the bad coupling between the temporary short-period seismography and surface combined with the narrowband characteristics of the instruments themselves, our receiver functions have higher noise levels than the broadband receiver functions. However, the dense array increases the resampling of velocity discontinuities by receiver functions; thus, the coherent signals can be greatly enhanced to suppress noise.

The distribution of seismic events affects the imaging results (Zheng et al., 2006). Figure 3 shows the epicenter distribution of our selected events. We can see that the events are mainly distributed in the east and southeast directions of the profile. So, we use the eastern direction as roughly being on the same great circle arc as our dominant direction. We then manually picked 1503 receiver functions for subsequent *H*-*κ* stacking and imaging. The selection criteria were that the P arrivals were clear and that the Pms phases could be continuously tracked in the receiver-function profiles of one event.

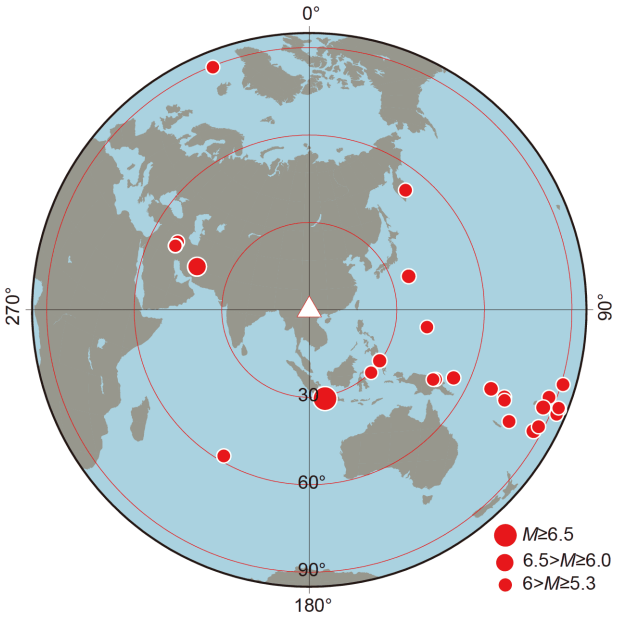

Figure 3 Locations of the research area and epicenters of 31 teleseismic events. Red solid circles: epicenter, white solid triangle: research area, and the circle sizes represent the magnitude.

2.3 *H*-*κ* stacking

The Poisson's ratio of crustal rocks is sensitive to their mineral compositions and can suggest whether the crust is partially melted or enriched with fluid (Mavko, 1980; Christensen, 1996). This crustal property can be obtained via seismic exploration and may help us understand crust-mantle structures and geodynamics. Zhu and Kanamori (2000) developed the *H*-*κ* stacking method to obtain the crustal thickness and average V_p/V_s ratio using a grid search assuming a horizontal interface. The Poisson's ratio of rocks

can be converted as

$$\sigma=0.5\times\left[1-(\kappa^2-1)^{-1}\right], \quad (1)$$

when a teleseismic P-wave hits the Moho, a Ps phase and its multiple phases PpPs and PsPs+PpSs are generated. The arrival times of the three phases are denoted as t_{Ps}, t_{PpPs}, and $t_{\mathrm{PsPs+PpSs}}$. The relationship between these three arrivals and three other physical parameters, namely the average velocity of the crustal P-wave (V_{p}), converted S wave (V_{s}), and the crustal thickness of (H) are described as follows.

$$H=\frac{t_{\mathrm{Ps}}}{\sqrt{V_{\mathrm{s}}^{-2}-p^2}-\sqrt{V_{\mathrm{p}}^{-2}-p^2}}, \quad (2)$$

$$H=\frac{t_{\mathrm{PpPs}}}{\sqrt{V_{\mathrm{s}}^{-2}-p^2}+\sqrt{V_{\mathrm{p}}^{-2}-p^2}}, \quad (3)$$

$$H=\frac{t_{\mathrm{PsPs+PpSs}}}{2\sqrt{V_{\mathrm{s}}^{-2}-p^2}}. \quad (4)$$

Because the ray parameter of every single receiver function is known, the theoretical arrival times of each phase can be estimated based on the above equations. Based on a given crustal thickness H, a given average $V_{\mathrm{p}}/V_{\mathrm{s}}$ ratio κ at a grid point, assumed average P-wave velocity and a continental $V_{\mathrm{p}}/V_{\mathrm{s}}$ ratio range of 1.7–2.0 (Christensen, 1996), the relationships between Ps arrival times and the PpPs/PsPs+PpPs arrival times are derived as follows:

$$\frac{t_{\mathrm{PpPs}}-t_{\mathrm{P}}}{t_{\mathrm{Ps}}-t_{P}}\approx 3\sim 3.85, \quad (5)$$

$$\frac{t_{\mathrm{PsPs}}-t_{\mathrm{P}}}{t_{\mathrm{Ps}}-t_{\mathrm{P}}}\approx 4\sim 4.85. \quad (6)$$

In general, the Ps phase is the clearest and easiest to identify and pick. For those receiver functions whose amplitudes of PpPs and PsPs+PpSs are weak, we can refer to the above empirical relationship. According to Zhu and Kanamori (2000), assuming that the velocity of a P-wave is known, for each given H and κ, we can obtain the theoretical arrivals of these three phases. Based on the arrivals, we can extract their corresponding amplitudes and stack them in terms of their weights,

$$S(H,\kappa)=\sum_{i=1}^{n}\omega_1 r_i(t_{\mathrm{Ps}})+\omega_2 r_i\left(t_{\mathrm{PpPs}}\right)-\omega_3 r_i\left(t_{\mathrm{PsPs+PpSs}}\right). \quad (7)$$

In eq. (7), $S(H,\kappa)$ is the objective function, $r_i(t)$ is the amplitude of the ith receiver function at time t. A regional crustal V_{p} of 6.3 km s^{-1} was adopted from wide-angle refraction/reflection studies (Bai and Wang, 2004; Wang et al., 2014) and from joint inversion of receiver functions and surface wave dispersions (Li et al., 2017). To emphasize the Ps phase arrivals, the amplitudes of the Ps, PpPs, and PsPs+PpSs phases were summed with weights of 0.6, 0.3, and 0.1, respectively. The grid search was performed for H within a range of 25–45 km with a step of 0.2 and for κ within a range of 1.6–1.9 km with a step of 0.05, respectively.

3. Imaging results of receiver functions

3.1 Receiver functions from different azimuths

According to the above procedure, we calculated and manually picked the time-domain receiver functions from the events shown in Figure 3. The piercing points of the ray paths on a horizontal plane at a depth of 38 km are depicted in Figure 4a. Figure 4b shows an example of the along-profile receiver functions from a well-recorded event in the dominant direction. Receiver functions from the same earthquake were sorted by station and plotted assuming equal station intervals. In the time-domain sections of the receiver functions, a continuous surface of the P-to-S conversions, interpreted as the Moho, appears between 4 and 5 s, which is shallow in the west but thick in the east. Also, between 2 and 3 s, there are local crustal positive phases which are relatively chaotic and are difficult to continuously track. A section of receiver functions stacked by station is shown in Figure 4c. We can see that the coherent signals were greatly enhanced and the noise was suppressed. The s phase became clearer and the crustal phases could be tracked continuously in the western part of the profile (e.g., station numbers from 1 to 280). In the eastern section of the profile after station number 300, the amplitudes of crustal seismic phases were weak and difficult to track. To track the continuous signals clearly and offer better noise suppression, we used the method proposed by Ward et al. (2018). Based on the distribution advantage of the dense array, receiver functions from adjacent stations were cross-correlated. We then selected those receiver functions whose cross-correlation coefficients were higher than 0.5 and performed a moving average of receiver functions over a window length of 5 km. As shown in Figure 4d, coherent signals were further enhanced and the lateral continuity was also improved.

3.2 *H*-κ stacking results

The H-κ stacking technique has been widely used in broadband receiver function studies (Sun et al., 2012; Wang et al., 2010; Wang X et al., 2018; Hu et al., 2005). It is important to consider that the observation duration using the short-period dense array only lasted slightly longer than a month and that the useful teleseismic events in a single station were limited. In this paper, we took advantage of the dense array and stored the receiver functions of the adjacent 31 stations for the middle stations. The receiver functions for the middle stations were used to perform H-κ stacking. This process produced the crustal thicknesses and the average $V_{\mathrm{p}}/V_{\mathrm{s}}$ ratios below the middle stations. We show an example of receiver functions sorted by epicentral distance (Figure 5a and 5b) and H-κ stacking results (Figure 5c and 5d) from two middle stations in the Lanping-Simao Basin along the western part of the profile and the results for the ALSRRSZ in the middle

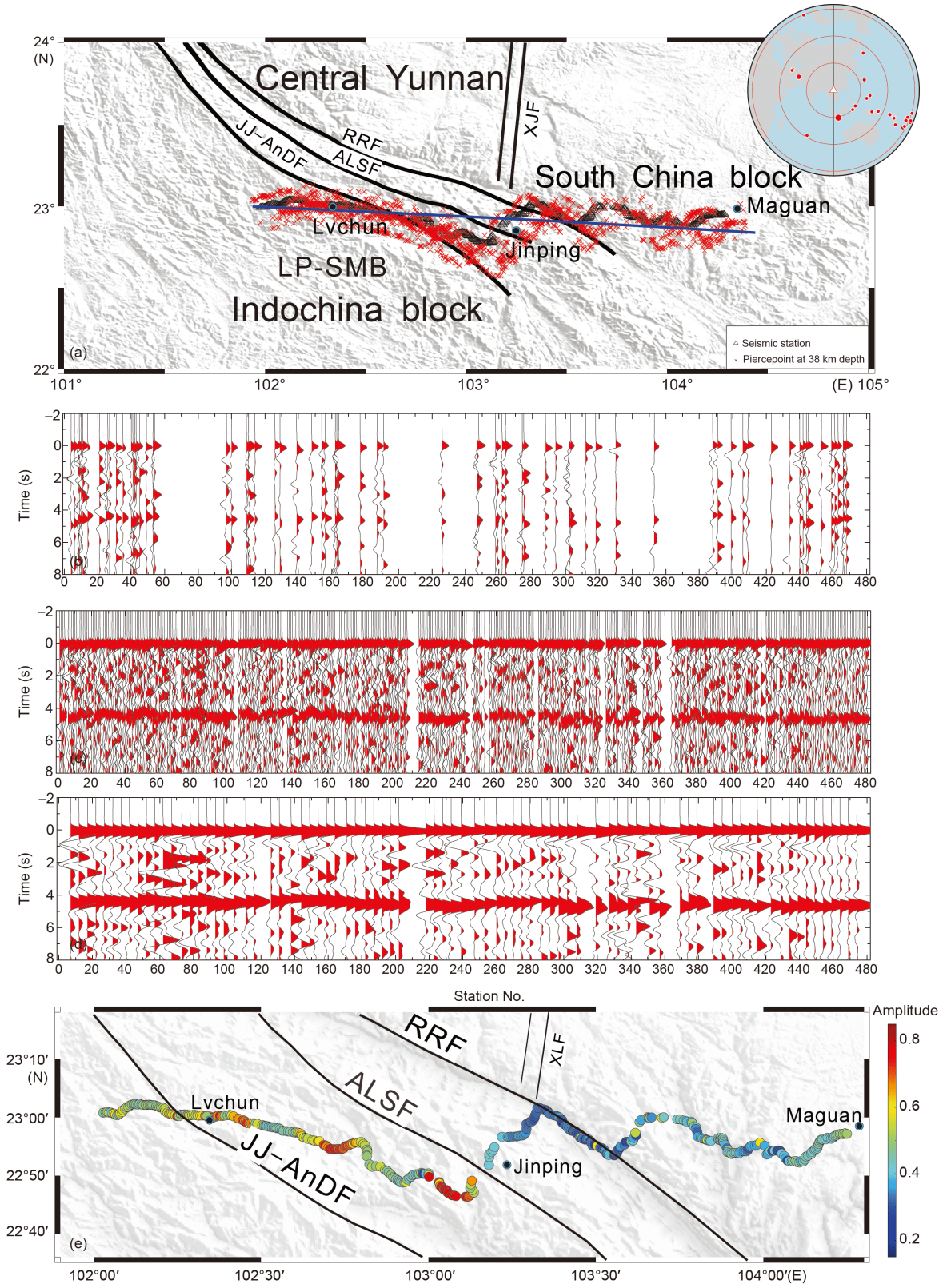

Figure 4 Piercing-point positions of the transmission points on the surface, amplitude variation diagram of the waveform profile of the receiving functions, and the Moho conversion wave. Panel (a) is the map of the distribution of piercing points at a depth of 38 km in which the black triangles represent the seismic stations, red crosses represent the piercing-point positions of the transmission points on the surface, and the blue line denotes the CCP stack profile. Panel (b) shows the section of the along-profile receiver functions whose epicenters are located in the dominant eastern direction. Panel (c) shows a section of the along-profile receiver functions stacked by station. Panel (d) shows a section of receiver functions after a moving average was applied with a window length of 5 km. In (b)–(d) the horizontal axis is the station number. Panel (e) shows the amplitude variations of the Moho Ps phase along the profile.

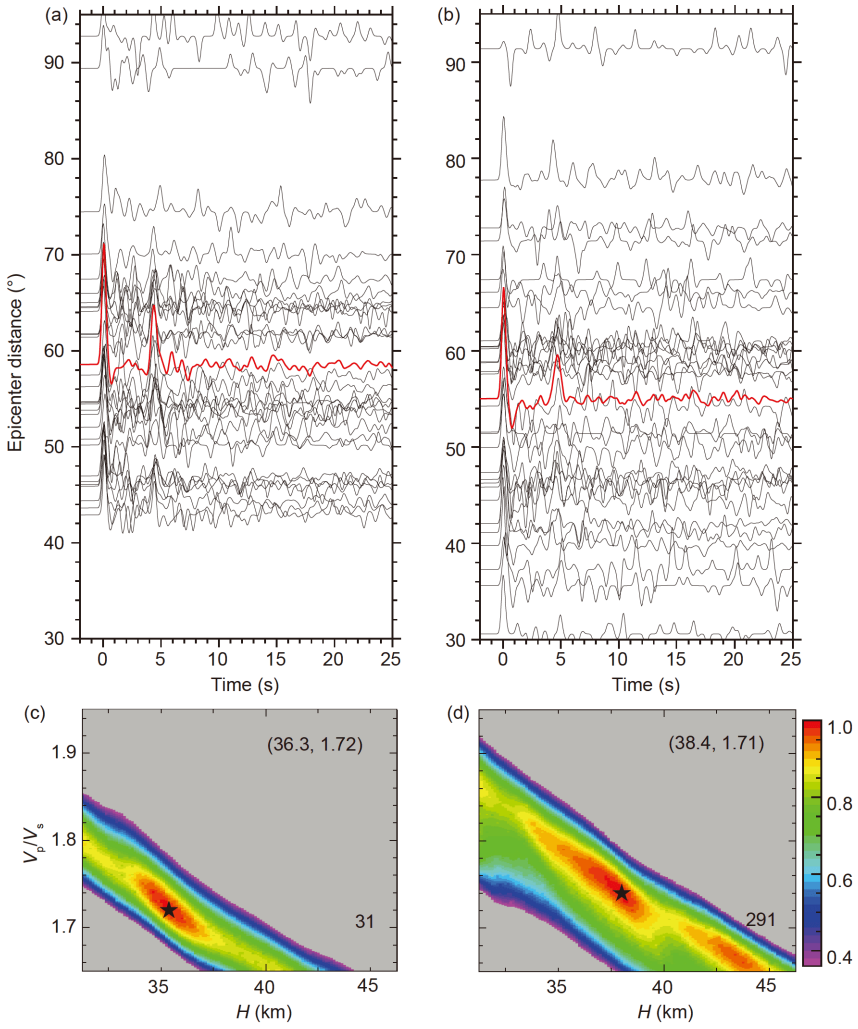

Figure 5 Examples of receiver functions sorted by epicentral distance and *H*-*κ* stacking results from two middle stations in the western and middle parts of the profile. The black thin solid lines represent receiver functions from different events and the red thick solid lines are the stacked traces of all receiver functions in panels (a) and (c). In panels (b) and (d), the black stars denote the extreme value of *H*-*κ* stacking, the numbers in the upper-right corners are the Moho depths and corresponding V_p/V_s ratios, and the numbers in the lower-right corners are the station numbers.

part of the profile. These figures show that the stacking results can converge to a stable extreme value within a reasonable range of crustal thicknesses and average V_p/V_s ratios, thus indicating the feasibility of traditional *H*-*κ* stacking for short-period, dense arrays. In the stacking results, there are some stations with large crustal thicknesses or jumps in V_p/V_s which may be caused by the weak multiples. A few of those stations were removed. Due to the small station interval, when the Moho depth or the average V_p/V_s ratio changed slightly, the lateral variation visually changed dramatically. So, we extracted the Moho depths and the average V_p/V_s ratios at every three stations and produced the profile of *H*-*κ* stacking (Figure 6b and 6c). As the results show, below the profile, the average Moho depth is approximately 37 km and is relatively thin in the west but is thicker in the east and these changes are roughly bounded by the ALSRRSZ. The average V_p/V_s ratio is 1.75, which is slightly lower than the global continental crustal average of 1.76 (Christensen, 1996). According to eq. (1), the average Poisson's ratio is approximately 0.25 (see Figure 6d). It is noteworthy that the average V_p/V_s ratio beneath ALSRRSZ is significantly greater.

3.3 Amplitude properties of Pms

The amplitude of the converted phase of the receiver function is an index for reflecting the property differences on both sides of an interface. Rychert et al. (2007) indicated that the velocity difference across two sides of an interface greatly affects the amplitude of the Ps phase. To investigate the physical properties of the Moho below the profile, we extracted the amplitude of the Pms converted phase of the receiver functions after stacking a single unit (Figure 4). During the calculation process, to obtain the lateral variation information of the converted energy wave of the Moho below the profile, we first stacked the receiver functions which

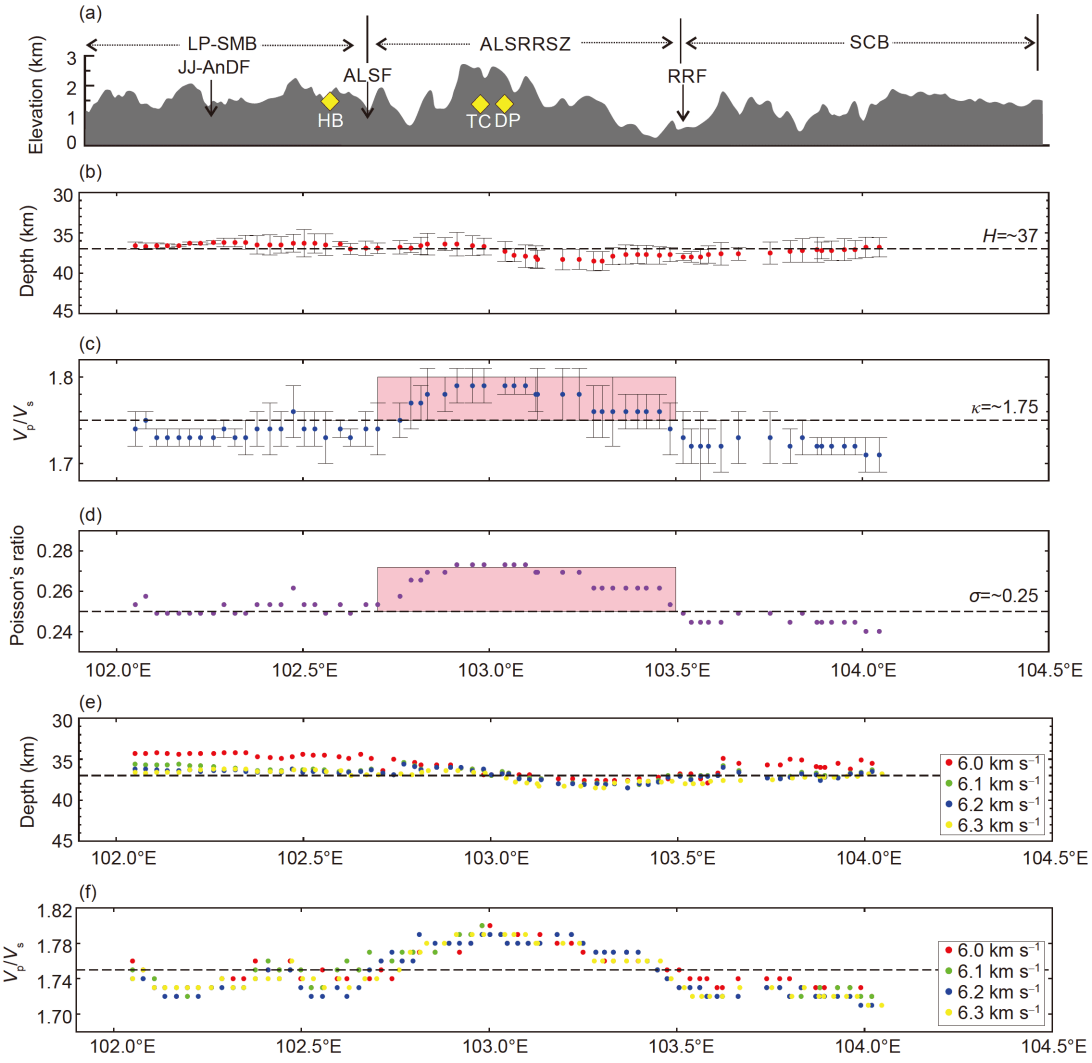

Figure 6 Graphs of Moho depth, average V_p/V_s ratio, and Poisson's e variations. (a) The elevations and tectonic divisions. LP-SMB, Lanping-Simao Basin; ALSRRSZ, Ailaoshan-Red River shear zone; SCB, South-China block; JJ-AnDF, Jiujia-Anding Fault; ALSF, Ailaoshan Fault; RRF, Red River Fault; HB, Habo ore deposit; TC, Tongchang ore deposit; DP, Daping ore deposit. (b) Crustal thickness changes, (c) V_p/V_s ratio changes, (d) Poisson's ratio changes. The pink boxes in panels (c) and (d) are used to highlight the range of anomalies in V_p/V_s ratios and Poisson's ratios. Panels (e) and (f) are the results of Moho depth H and V_p/V_s ratios κ when V_p ranges from 6.0 to 6.3 km s^{-1}.

connected multiple events (e.g., time domain stack). Moreover, considering some beneficial factors such as the high station density and the small differences in variations of the structural changes for the short lateral distances near the Moho, we conducted moving average processing on the receiver functions after stacking all of the time domains of the profiles by using a window length of 5 km (Ward et al., 2018) (e.g., space stack) to obtain stable amplitudes of the converted phase from the Moho. We also extracted the Pms amplitude of the converted phase of the receiver functions after moving average processing relative to the amplitudes of the direct P waves to create a visual display of the lateral energy variations. This normalization was conducted for each receiver-function relative to its own P-wave amplitude. The amplitudes of the converted phase from the Moho are shown in Figure 4e and we can see the obvious amplitude characteristics below the Ailaoshan-Red River shear zone.

3.4 Stack imaging of common conversion points

Owing to the short observing duration, limited event numbers, and patchy azimuth coverage, we chose the events on the east side (which are consistent with the survey lines) for investigation with CCP imaging. Choosing the narrow-azimuth seismic events helps to reduce the effects of uneven distributions of earthquake locations, dip interfaces, and anisotropy (Zheng et al., 2006). When the seismic events are distributed along the strike of the profile, the ray penetration points are nearly below the profile and may be able to better reflect the structure below the stations. This article used the IASP91 reference model for the transformation of receiver functions from the time domain to the depth domain. The

mesh size used for stack imaging was 40 km×2 km×1 km (e.g., the direction perpendicular to the survey lines, direction along the profile, and vertical direction, respectively).

The imaging results of seismic events arriving from east of the profile are shown in Figure 7b. The undulating shape of the Moho agrees well with the results from *H*-*κ* stacking (e.g., the red points in Figure 6b and the bold black dots in Figure 7); the average depth of the Moho is approximately 37 km. The Moho under the Lanping-Simao Basin is the shallowest at about 36 km and the Moho below Ailaoshan-Red River shear zone is the deepest at approximately 39 km and exhibits a dislocated landform. In the eastern segment of the Red River Fault, the Moho begins to slightly rise upward. The imaging results show that there are obvious horizontally non-continuous high-velocity discontinuities in the crust, which are located at depths of 5–10 and 15–25 km. For the South-China blocks in the eastern part of the Red River Fault, the crustal interfaces are relatively flat. The two high-velocity discontinuities slope slightly to the west between the Red River Fault and Ailaoshan Fault. For the Indochina block in the western part of the Ailaoshan Fault, the high-velocity discontinuity surfaces within the crust all bend toward the middle crust. Meanwhile, as was described in the previous section, the arrival times of the PpPs seismic phase are approximately 3–4 times those of the Ps seismic phase. We also saw the multiple-wave signals of these two phases from depths of approximately 45–50 and 55–65 km.

Generally, there are sedimentary structures in the shallow surface which are characterized by low velocities; also there are no obvious velocity changes on both sides of the underlying crystalline basement. These produce strong converted wave signals. These signals oscillate between the free surface and the crystalline basement and interfere with the converted waves produced by the other velocity discontinuities and by the Moho. The multiples of the Ps converted wave at the shallow interfaces affect the phases of subsequent seismic phases. Meanwhile, when the arrival times of the multiples are the same as those of the converted wave from the deep interface, the Ps wave amplitudes from the deep interface are either enhanced or inhibited. A synthetic receiver function is displayed in Figure 8 and is based on a simple crustal model based on different thickness of the

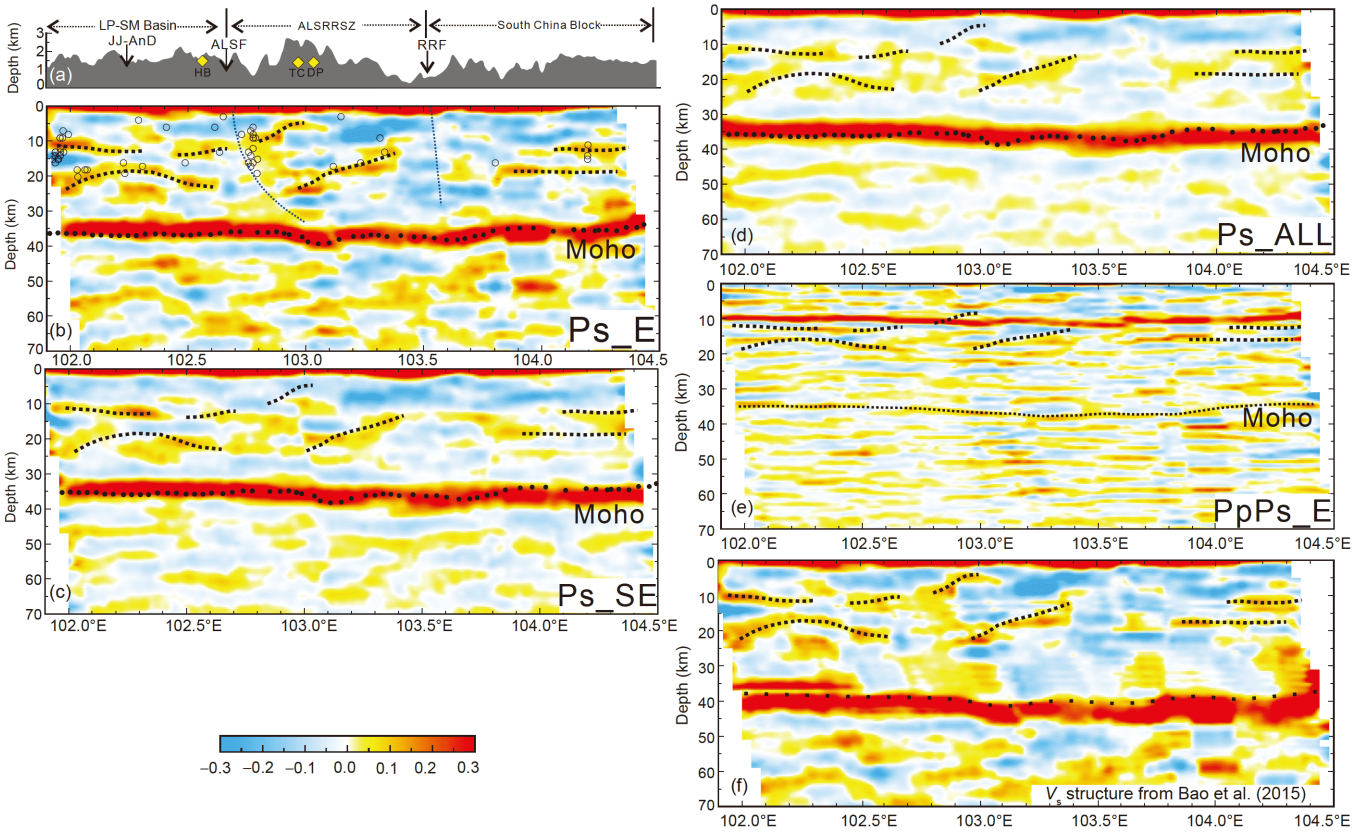

Figure 7 The results of CCP stack imaging. The elevations along the profile in (a) (the same with Figure 6). Panels (b) and (c) represent the Pms imaging results of the seismic events arriving from the east and southeast directions, respectively. The black hollow circles in (b) represent those seismic events with magnitudes greater than 2.0 for the area within 5 km of both sides of the profile from 2001 to 2018. The black solid dots are the depth results of the Moho obtained using *H*-*κ* stacking. The two dotted lines represent the speculative deep shapes of the Ailaoshan and Red River Faults. The morphological features refer to Li et al. (2016). Panel (d) shows the imaging results of the seismic events from all locations. Panel (e) shows the imaging results from the PpPs multiple waves for the seismic events arriving from the east. The letters in the bottom right corner of each figure represent the locations of the phase for imaging and the particular seismic events. Panel (f) displays the Ps imaging results for the seismic events arriving from east of the profile and the V_s velocity is referred to Bao et al. (2015).

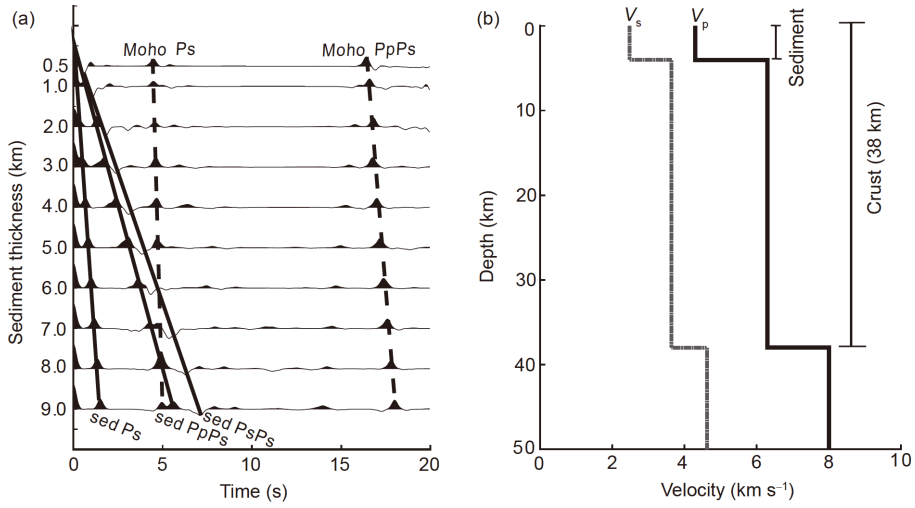

Figure 8 The effects of crystalline basement on receiver functions. (a) The theoretical receiver functions for different thicknesses of sedimentary layers in which the reference ray parameter is 0.06 km s^{-1}. The tilted solid line represents the associated seismic phase from the sedimentary layer and the dotted line represents the associated seismic phase from the Moho. (b) The velocity model used.

sedimentary layer for which the depth of the Moho is fixed at 38 km. Clearly, the multiples of the shallow interface cause great differences to the subsequent phases. When the multiples appear inside the crust, the Ps phase from the Moho will visually appear to move backward. Moreover, the multiples suppress the amplitudes of the Ps phase from the Moho (e.g. when H_{sediment}=6 km) which leads to difficulties in distinguishing the Ps phase from the Moho.

To confirm that the interface inside the crust observed in our study is a real geological structure instead of multiple-wave illusions from shallow crustal interfaces, we performed multiple-wave imaging by using the receiver functions for the seismic events from the eastern direction of the profile. The results are displayed in Figure 7e and are similar to the results of the Pms imaging shown in Figure 7b. The corresponding depths of the crustal interface in the imaging results also exist in the multiple-wave imaging results. If these interfaces were multiple-wave illusions, then the multiples would be repositioned to the shallow interface. This demonstrates that the two groups of seismic phases observed within the crust are from real crustal structures.

In addition, we conducted similar Ps phase imaging using the seismic events from the eastern direction of the profile and using all directions. The results are shown in Figure 7c and 7d, respectively. The Moho and main interface within the crust are very similar to the interface morphology as shown in Figure 7b, which demonstrates that our imaging results are stable and reliable. Because of the influence of the distribution of the seismic events, some local features in the imaging, such as the amplitudes of the seismic phases, are different from the results of the events from the eastern direction of the profile. However, these differences have little effect on the interface-depth information.

4. Results and discussion

4.1 The distribution of V_p/V_s ratios along the profile and CCP imaging results

Based on *H*-*κ* stacking and CCP imaging of teleseismic P-wave receiver functions, we obtained V_p/V_s ratio variations, crustal thicknesses, and fine geometric structures inside the crust below the profile. We also determined the lateral variations of the converted wave between the crust and mantle along the profile by extracting the amplitude properties of the Pms phase from the Moho. First of all, the results of V_p/V_s ratios and Poisson's ratios (Figure 6c and 6d) indicate that the average V_p/V_s ratio is 1.75, which is slightly lower than the average value of global continents. It reveals the high value anomaly below the Ailaoshan-Red River shear zone which is higher than those in the South-China and Indochina blocks on east and west sides; this anomaly indicates that there are differences in physical properties between the area below Ailaoshan-Red River shear zone and the blocks on both sides. Our *H*-*κ* stacking results based on observation data by dense seismic array are consistent with earlier studies conducted at large scales (Li et al., 2009; Xu et al., 2006). Moreover, the average V_p/V_s ratio (1.79) of the crust below the Ailaoshan-Red River shear zone disclosed by the high-resolution image is close to Hu et al.'s (2018) results, which verifies the credibility of our results. The difference is that Hu et al.'s (2018) results were calculated by using the data from fixed stations with wide station spacing whose lateral resolution was greater than 30 km. A local high Poisson's ratio anomaly was indicated only near the intersection of 23°N and the Red River Fault. By comparison, our results showed that the local high V_p/V_s ratio anomaly (1.79) is very similar to the topographic height of Ailao Mountain. This anomaly is confined to the Ailaoshan Fault in the west and

Red River Fault in the east. We infer that magmatic hydrothermal fluids or abundant ferromagnesian minerals (Tarkov and Vavakin, 1982) may exist in the crust below the shear zone. The evidence of a weak Pms phase from the Moho (see Figure 4e) and the distribution of high surface heat value (Wang Y et al., 2018) suggest that there is hydrothermal material and energy exchange between the crust and mantle.

Bao et al. (2015) and Qiao et al. (2018) showed that a mid-lower crustal low velocity layer exists at the intersection of the Red River and Xiaojiang Faults. To confirm whether this low velocity layer has any effect on our *H*-κ scanning results, we conducted *H*-κ stacking based on different V_p values (Figure 6e and 6f). These results show that the computed Moho depths and V_p/V_s ratios from different V_p generally have the same variation tendency. The areas beneath Ailao Mountain are all characterized by subsidence of the Moho and the V_p/V_s ratio is definitely high, which explains that the stacking results were less affected by the average velocity V_p. Therefore, our *H*-κ results from V_p, which are based on wide-angle refractions/reflections (Bai and Wang, 2004; Wang et al., 2014) are reliable.

The combination of CCP imaging results and the thickness of the Moho obtained by *H*-κ stacking shows that the average thickness of the crust is approximately 37 km, which is close the wide-angle refraction/reflection results for this particular area and adjacent areas (Bai and Wang, 2004; Wang et al., 2014) and receiver-function observations (Li et al., 2009; Xu et al., 2007; Wang et al., 2010; Li et al., 2017). At 103°E on the east side of Ailaoshan Fault, there is an obvious fault dislocation phenomenon at the Moho boundary. Therefore, we infer that the Ailaoshan Fault may be a deep, large-scale fault which cuts through the Moho. There is a mirror image relationship between the overall subsidence morphology of the Moho below the Ailaoshan-Red River shear zone and Ailao Mountainthe topography of Ailao Mountain with an uplifted surface; this indicates that the gravity driven isostatic effect on the orogenic process cannot be neglected. This article used the IASP91 global reference-velocity model to conduct the time-depth conversions of receiver functions. Considering the complex configurations of the regional crustal structure, we also referred to Bao et al.'s (2015) V_s velocity model to compute the average 1D V_p reference velocity in this area. We performed CCP imaging of the Ps converted waves of the seismic events in the eastward azimuth (see Figure 7f). Compared with the results in Figure 7b, the interface characteristics of the middle-upper crust are basically the same. The only difference is that the Moho in Figure 7f is deeper than that in Figure 7b. However, this difference in the models did not influence our analysis of relevant geological structures and deep geodynamic processes in this area.

Compared with broadband seismic arrays, short-period dense seismic arrays provide a better illumination function for the crustal interior and have been applied successfully in the northeastern margin of the Tibetan Plateau (Liu et al., 2017). Our results display the fine structure characteristics of the discrete high-velocity discontinuous surface within the crust, whose characteristics are consistent with earlier wide-angle refraction/reflection results (Bai and Wang, 2004; Zhang et al., 2007; Deng et al., 2011). We vertically divided the crust into upper, middle, and lower layers. Laterally, using the Ailaoshan and Red River Faults as tectonic boundaries, we divided this area into three parts: the Indochina block on the west, Ailaoshan-Red River shear zone in the middle, and South-China block on the east. The curved interface on the west side of the crust reflects the existence of strong transverse extrusion stress. Its curved shape also suggests that the crust in this region may be a relatively weak layer. In the middle, the interface inside the crust below the Ailaoshan-Red River shear zone underwent oblique deformation whose geometry conformed satisfied with the Cenozoic kinematic model of the Diancang Mountain-Ailao Mountain, which indicated that this area had experienced oblique uplifting since the Pliocene, as proposed by Li et al. (2012). There are large areas with weak reflections below the inclined interface and near the Red River Fault, which may suggest that the crustal materials due to magmatic underplating from upper mantle were not completely differentiated. The interfaces inside the crust did not undergo any obvious deformation under the South-China block in the east. Some significant differences were found in the crustal deformations on both sides of the Red River Fault. All of these features suggest that the Red River Fault, as a plate boundary zone, is a deep, large-scale fault.

4.2 Nowadays geodynamic status of the Ailaoshan-Red River shear zone

As we know, the role of the Red River Fault zone in regional tectonic evolution has always attracted the attention of Chinese and foreign scholars(e.g. Leloup et al., 1995; Li et al., 2001). Liang et al. (2007) proposed that Ailaoshan-Red River shear zone began to activate at least 36 Ma. Tapponnier et al. (1990) believed that the Ailaoshan-Red River shear zone stopped at 23 Ma. A large amount of literature shows that the Red River Fault has experienced a large-scale left-lateral strike-slip since the Cenozoic and nowadays exhibits a right-lateral strike-slip feature. It was characterized as a left-lateral strike-slip fault before approximately 21 Ma with a sliding distance of 400–500 km (Zhong and Ding, 1996; Leloup et al., 1993) and it has been in a dextral strike-slip state since approximately 5 Ma (Leloup et al., 1995). Liu et al. (2011) pointed out that strong orogeny occurred in the Ailao Mountain area during the Paleocene, late Oligocene, and early Miocene. Wang et al. (2006) stated that regional uplifts occurred at 22–17, 13–9, and ~5 Ma, respectively in

the Diancang Mountain and Ailao Mountain areas since the Cenozoic era. By contrast, Li et al.'s (2016) study of river terrace ages showed that the Red River Fault/shear zone had undergone two periods of uplift since the Pliocene; the tectonic uplift at approximately 3.6 Ma is the strongest and the uplift rate has been increasing since 2.6 Ma. Based on the results of $^{40}Ar/^{39}Ar$ and apatite fission track chronology, Li et al. (2012) assumed that the Diancang Mountain-Ailao Mountain area has experienced oblique uplifting since 5–3 Ma, which is characterized by large uplift amplitudes in the east and smaller uplift amplitudes in the west.

Our imaging results from the receiver functions showed that there are two obvious inclined interfaces in the middle and upper crust beneath the Ailao Mountain (Figure 7b), this observation result supports the perspective that Ailao Mountain has experienced an oblique uplifting. The apparent subsidence of the Moho below Ailao Mountain implies the gravity isostasy caused by the uplifting of the mountain range. The evidence, such as the weak Pms energy of the converted phase of the Moho below Ailao Mountain (Figure 4e), broken reflection structures within the crust indicated by the interfaces, and distributions of high surface heat flux and hot springs (Wang Y et al., 2018), together with the previous research results such as the lower Pn wave velocities in the lower part of the this area (Lei et al., 2009) and the obvious low velocity anomaly in upper mantle (Li et al., 2008; Xu X M et al., 2015; Zhang et al., 2018) all indicate that there is a significant heat source in the upper mantle around this area, which suggests that the crust-mantle magmatic hydrothermal activity related to orogenic processes have not stopped and could attributed to the partial melting of the crustal rock. Therefore, we deduce that the diapir of mantle-sourced magma in the crust (which is clearly stronger than that in the West) together with the lateral collision of the Indian plate led to the oblique uplifting of Ailao Mountain area since the Cenozoic era.

Meanwhile, the uplifting differences caused by tectonic movements at different stages of the Red River Fault may play an important role. Li et al.'s (2018) study on the fault-slip rate study based on GPS measurements from 1997 to 2017 showed that the upward dip rate of the Red River Fault near the profile (23°N) may amount to 2 mm yr^{-1}, which indicates that the tectonic movement on the south part of Red River Fault still has a large thrust component. This result also provides us some evidence for the above interpretation.

4.3 Magma-fluid-metallogenic systems in Ailao Mountain area

In the Ailao Mountain area, porphyry copper-gold deposits such as Tongchang and Habo and orogenic gold and polymetallic deposits such as Daping and Chang'an have developed since the Cenozoic. Their metallogenic mechanisms, deep geodynamic processes, and relationships with the regional tectonic evolution have long attracted the attention of scholars (Sun et al., 2007; Chen, 2013; Tian et al., 2014; Deng et al., 2013; Hou et al., 2017). Zhu et al. (2009) considered that the genesis of the deposits had a relationship with the stretching which took place after the collision and intra-crust magma and fluids caused by intracontinental transform orogenic movements. Ge et al. (2009) proposed that the Ailao Mountain polymetallic ore deposits have a unified deep structural background and that the three-episode uplift of the asthenosphere from the late Paleozoic controlled the tectonic activity, diagenetic and metallogenic processes in the shear zone. Yuan et al.'s (2010) study on isotope compositions in the Daping super-large gold deposit showed that strong, deep magmatic activity occurred during the formation process of the Ailao Mountain mineral belt, and the interaction of the crust and mantle greatly affected the formation of these deposits.

There is a consensus among scholars on the existence of fluids and magmatic hydrothermal fluids in the Ailao Mountain metallogenic belt. Some have even considered that the fluids from the deeper zones were involved in the ore-forming processes (Ge et al., 2010). Generally, the high V_p/V_s ratios are related to the fluids or mafic components in the crust.

Our H-κ stacking results showed that the high V_p/V_s ratio anomaly is as high as 1.79 below the Ailao Mountain area. Combined with the evidence of a low velocity anomaly in the upper mantle (Li et al., 2008; Xu X M et al., 2015; Zhang et al., 2018) and the distribution of high surface heat fluxes and hot springs (Wang Y et al., 2018) (introduced before), there may be uncooled magma hydrothermal fluids from the upper mantle or exist rock partial melting in the crust.

The southern Ailao Mountain ore concentration area is located on both sides of the Ailaoshan Fault (Figure 7a). Based on the fault position at the surface, Moho dislocation, uplift and offset of crustal interfaces, surface elevation variations, and the hypocenter distributions of small earthquakes along the profile (Figure 7b), we suggest that both the Red River and Ailaoshan Faults are deep, large-scale faults. The Red River Fault is considered to be a high-angle northeast-trending fault, while the Ailaoshan strike-slip fault may be a strike-slip fault which trends to northeast and extends to the lower crust; this fault may even cut through the Moho. The Ailaoshan Fault may act as a conduit for upgoing magma and fluids. It has controlled the magmatic activity and mineralization of the Ailao Mountain area since the Cenozoic. Mao et al. (2005) assumed that the fast convergence of Indo-Eurasian plate led the rapidly rising of Ailao Mountain in 35–40 Ma. They also deduced that alkali-rich porphyry magma with crust-mantle property was originated from the decompression and melting of the lower mantle, and a series

of porphyry copper deposits were accumulated and formed at proper locations due to the differential evolution of magma raised up along deep faults. Our CCP imaging results show that there is an obvious inclined subsurface beneath Ailao Mountain, which supports the above-mentioned understanding of the uplift of Ailao Mountain since the Cenozoic. The Moho offset below Ailao Mountain indicates that the Ailaoshan Fault may cut through the Moho and extend to the top of the upper mantle. Below the ALSRRSZ, the weak amplitude of the Pms phase from the Moho and the high average crustal V_p/V_s ratio anomaly suggest the exchange of magma or hot materials between the crust and mantle and that the crust is rich in fluids and mafic minerals. This supports above view of the ore-forming process that the porphyry copper deposits in this area were mainly formed due to the differential evolution of alkali-rich porphyry magma went up along deep faults(Mao et al., 2005).

5. Conclusions

(1) The greatest thickness (up to 39 km) and highest average V_p/V_s ratio (the maximum value is 1.79) of the crust of the Ailao Mountain area indicate that the ALSRRSZ is rich in fluids and mafic components. This offers direct geophysical evidence to study the remarkable tectonics and mineralization which have occurred since the Cenozoic around the Ailao Mountain area.

(2) The evidence of a weak Pms phase from the Moho and broken reflection crustal structures, together with the high surface heat values and low P-wave velocities in the upper mantle, imply strong interactions between the crust and mantle beneath the ALSRRSZ. In addition, there are inclined crustal interfaces beneath the ALSRRSZ which reveal the uneven uplift characteristics of Ailao Mountain since the Cenozoic era. The formation of inclined crustal interfaces may have a relationship with several factors, such as the diapir of upgoing magma from the upper mantle below Ailao Mountain (the diapir is stronger in the east than in the west) as well as the differential uplift caused by the squeezing action from the lateral collision of the Indian plate and the strike-slip movement of the Red River Fault.

(3) Based on the geophysical evidence presented in this article, we consider that the Ailaoshan Fault is a deep, large-scale fault which extends to the upper mantle. Since the Cenozoic, it has played an ore-conducting role by controlling the spatial distribution of the Ailao Mountain mineralization belt.

Acknowledgements *We acknowledge the two anonymous reviewers for their constructive comments and suggestions. We thank the Short-period Seismic Array Laboratory of IGGCAS and the Geophysical Exploration Center, China Earthquake Administration for collecting the data. Helpful discussions and suggestions from Professor Laicheng Miao of IGGCAS are sincerely acknowledged. This work was supported by the National Key Research and Development Program of China (Grant No. 2016YFC0600302), the Second Tibetan Plateau Scientific Expedition and Research Program (STEP) (Grant No. 2019QZKK0701), and the National Natural Science Foundation of China (Grant Nos. 41774097, 41674064, 41704042 & 41574082).*

References

Avouac J P, Tapponnier P. 1993. Kinematic model of active deformation in central Asia. Geophys Res Lett, 20: 895–898

Bai Z M, Wang C Y. 2004. Tomography research of the Zhefang-Binchuan and Menglian-Malong wide-angle seismic profiles in Yunnan province (in Chinese). Chin J Geophys, 47: 257–267

Bao X W, Sun X X, Xu M J, Eaton D W, Song X D, Wang L S, Ding Z F, Mi N, Li H, Yu D Y, Huang Z C, Wang P. 2015. Two crustal low-velocity channels beneath SE Tibet revealed by joint inversion of Rayleigh wave dispersion and receiver functions. Earth Planet Sci Lett, 415: 16–24

Chen L, Wen L X, Zheng T Y. 2005. A wave equation migration method for receiver function imaging: 1. Theory. J Geophys Res, 110: B11309

Chen Y J. 2013. The development of continental collision metallogeny and its application (in Chinese). Acta Petrol Sin, 29: 1–17

Christensen N I. 1996. Poisson's ratio and crustal seismology. J Geophys Res, 101: 3139–3156

Cong Y, Dong Q J, Xiao K Y. 2013. Study on metallogenic model and ore exploration of porphyry deposits in Sanjiang metallogenic belt (in Chinese). J Geol, 37: 562–569

Deng J, Ge L S, Yang L Q. 2013. Tectonic dynamic system and compound orogeny: Additionally discussing the temporal-spatial evolution of Sanjiang orogeny, Southwest China (in Chinese). Acta Petrol Sin, 29: 1099–1114

Deng Y F, Li S L, Fan W M, Liu J. 2011. Crustal structure beneath South China revealed by deep seismic soundings and its dynamic implications (in Chinese). Chin J Geophys, 54: 2560–2574

Fu Y Y V, Gao Y, Li A B, Li L, Chen A G. 2017. Lithospheric structure of the southeastern margin of the Tibetan Plateau from Rayleigh wave tomography. J Geophys Res-Solid Earth, 122: 4631–4644

Ge L S, Deng J, Guo X D, Zou Y L, Liu Y C. 2009. Deep-seated structure and metallogenic dynamics of the Ailaoshan polymetallic mineralization concentration area, Yunnan Province, China. Sci China Ser D-Earth Sci, 52: 1624–1640

Ge L S, Deng J, Yang L Q, Yuan S S, Guo C Y. 2010. Evolution of tectonic environment and gold-polymetal metallogenic system in Ailaoshan ore concentration region, Yunnan province, China (in Chinese). Acta Petrol Sin, 26: 1699–1722

Hou Z Q, Zhong D L, Deng W M. 2004. A tectonic model for porphyry copper-molybdenum-gold metallogenic belts on the eastern margin of the Qinghai-Tibet Plateau (in Chinese). Chin Geol, 31: 1–14

Hou Z Q, Zhou Y, Wang R, Zheng Y C, He W Y, Zhao M, Evans N J, Weinberg R F. 2017. Recycling of metal-fertilized lower continental crust: Origin of non-arc Au-rich porphyry deposits at cratonic edges. Geology, 45: 563–566

Hu J F, Su Y J, Zhu X G, Chen Y. 2005. S-wave velocity and Poisson's ratio structure of crust in Yunnan and its implication. Sci China Ser D-Earth Sci, 48: 210

Hu J F, Badal J, Yang H Y, Li G Q, Peng H C. 2018. Comprehensive crustal structure and seismological evidence for lower crustal flow in the southeastern margin of Tibet revealed by receiver functions. Gondwana Res, 55: 42–59

Langston C A.1977. The effect of planar dipping structures on the source and receiver for constant ray parameter. Bull Seismol Soc Am, 67: 1029–1050

Lei J S, Zhao D P, Su Y J. 2009. Insight into the origin of the Tengchong intraplate volcano and seismotectonics in southwest China from local

and teleseismic data. J Geophys Res, 114: B05302
Leloup P H, Harrison T M, Ryerson F J, Wenji C, Qi L, Tapponnier P, Lacassin R. 1993. Structural, petrological and thermal evolution of a Tertiary ductile strike-slip shear zone, Diancang Shan, Yunnan. J Geophys Res, 98: 6715–6743
Leloup P H, Lacassin R, Tapponnier P, Schärer U, Zhong D, Liu X, Zhang L, Ji S, Trinh P T. 1995. The Ailao Shan-Red River shear zone (Yunnan, China), Tertiary transform boundary of Indochina. Tectonophysics, 251: 3–84
Li B L, Ji J Q, Luo Q H, Gong J F, Qing J C. 2012. The structure style and timing of uplift of the Ailaoshan-Diancangshan range, west Yunnan, China (in Chinese). Seismol Geol, 34: 696–712
Li C, van der Hilst R D, Meltzer A S, Engdahl E R. 2008. Subduction of the Indian lithosphere beneath the Tibetan Plateau and Burma. Earth Planet Sci Lett, 274: 157–168
Li C J, Gan W J, Qin S L, Hao M, Song S W. 2018. Present-day activity of the main active faults in central Yunnan area (in Chinese). J Seismol Res, 41: 381–389
Li C Y, Jiang X D, Li D Y, Gong W, Bi C L. 2016. Tectonic uplift and its regime in the central southern Segment of the Red River fault zone since Pliocene (in Chinese). Period Ocean Univ China, 46: 090–098
Li Q, Chen W J, Wan J L. 2001. New evidence of tectonic uplift and transform of movement style along Ailao Shan-Red River shear zone. Sci China Ser D-Earth Sci, 44: 124–132
Li Y H, Wu Q J, Tian X B, Zhang R Q, Pan J T, Zeng R S. 2009. .Crustal structure in the Yunnan region determined by modeling receiver functions (in Chinese). Chin J Geophys, 52: 67–80
Li J T, Song X D, Zhu L P, Deng Y F. 2017. Joint inversion of surface wave dispersions and receiver functions with P velocity constraints: Application to southeastern Tibet. J Geophys Res-Solid Earth, 122: 7291–7310
Liang H Y, Campbell I H, Allen C M, Sun W D, Yu H X, Xie Y W, Zhang Y Q. 2007. The age of the Potassic alkaline ingenous rocks along the Ailao Shan-Red River shear zone: Implications for the onset age of left-lateral shearing. J Geol, 115: 231–242
Ligorria J P. Ammon C J. 1999. Iterative deconvolution and receiver-function estimation. Bull Seismol Soc Am, 89: 1395–1400
Liu F T, Liu J H, He J K, You Q Y. 2000. The subduction plate of the lower Yangtze block beneath the Tethys orogenic, west Yunnan (in Chinese). Chin Sci Bull, 45: 79–85
Liu J L, Tang Y, Song Z J, Tran M D, Zhai Y F, Wu W B, Chen W. 2011. The Ailaoshan belt in western Yunnan: Tectonic framework and tectonic evolution (in Chinese). J Jinlin Univ-Earth Sci, 41: 1285–1303
Liu Z, Tian X B, Gao R, Wang G C, Wu Z B, Zhou B B, Tan P, Nie S T, Yu G P, Zhu G H, Xu Z. 2017. New images of the crustal structure beneath eastern Tibet from a high-density seismic array. Earth Planet Sci Lett, 480: 33–41
Mavko G M. 1980. Velocity and attenuation in partially molten rocks. J Geophys Res, 85: 5173–5189
Mao J W, Li X F, Li H M, Qu X M, Zhang C Q, Xue J C, Wang Z L, Yu J J, Zhang Z H, Feng C Y, Wang R Y. 2005. Types and characteristics of endogenetic metallic deposits in orogenic belts in China and their metallogenic processes (in Chinese). Acta Geol Sin, 79: 342–372
Owens T J, Zandt G, Taylor S R. 1984. Seismic evidence for an ancient rift beneath the Cumberland Plateau, Tennessee: A detailed analysis of broadband teleseismic *P* waveforms. J Geophys Res, 89: 7783–7795
Pan S Z, Wang F Y, Duan Y H, Deng X G, Song Z H, Duan Y L, Sun Y N, Zhang C J, Yang Y D, Zang Y R. 2015. Basement structure of southern Yunnan and adjacent areas: The Zhenkang-Luxi deep seismic sounding profile (in Chinese). Chin J Geophys, 58: 3917–3927
Peltzer G, Tapponnier P. 1988. Formation and evolution of strike-slip faults, rifts, and basins during the India-Asia Collision: An experimental approach. J Geophys Res, 93: 15085–15117
Qiao L, Yao H, Lai Y C, Huang B S, Zhang P. 2018. Crustal structure of southwest and northern Vietnam from ambient noise tomography: Implications for the large-scale material transport model in SE Tibet. Tectonics, 37: 1492–1506
Rychert C A, Rondenay S, Fischer K M. 2007. P-to-S and S-to-P imaging of a sharp lithosphere-asthenosphere boundary beneath eastern North Ameirca. J Geophys Res, 112: B08314
Royden L H. 1996. Coupling and decoupling of crust and mantle in convergent orogens: Implications for strain partitioning in the crust. J Geophys Res, 101: 17679–17705
Sun X L, Sun W D, Hu Y B, Ding W, Ireland T, Zhan M Z, Liu Ji Q, Ling M X, Ding X, Zhang Z F, Fan W M. 2018. Major Miocene geological events in southern Tibet and eastern Asia induced by the subduction of the Ninetyeast Ridge. Acta Geochem, 37: 395–401
Sun X M, Xiong D X, Shi Y G, Wang S W, Zhai W. 2007. $^{40}Ar/^{39}Ar$ dating of gold deposit hosted in the Daping ductile shear zone in the Ailaoshan gold belt (in Chinese). Acta Geol Sin, 81: 88–92
Sun Y, Niu F L, Liu H F, Chen Y L, Liu J X. 2012. Crustal structure and deformation of the SE Tibetan plateau revealed by receiver function data. Earth Planet Sci Lett, 349-350: 186–197
Tapponnier P, Molnar P. 1977. Active faulting and tectonics in China. J Geophys Res, 82: 2905–2930
Tapponnier P, Peltzer G, Le Dain A Y, Armijo R, Cobbold P. 1982. Propagating extrusion tectonics in Asia: New insights from simple experiments with plasticine. Geology, 10: 611–616
Tapponnier P, Lacassin R, Leloup P H, Scharer U, Zhong D L, Wu H W, Liu X H, Ji S C, Zhang L S, Zhong J Y. 1990. The Ailao Shan/Red River metamorphic belt: Tertiary left-lateral shear between Indochina and South China. Nature, 343: 431–437
Tarkov A P, Vavakin V V. 1982. Poisson's ratio behaviour in various crystalline rocks: Application to the study of the Earth's interior. Phys Earth Planet Inter, 29: 24–29
Tian G, Zhang C Q, Peng H J, Zhou Y M, Li J R, Zhang X P, Hu M Y. 2014. Petrogenesis and geodynamic setting of the Chang'an gold deposit in southern Ailaoshan metallogenic belt (in Chinese). Acta Petrol Sin, 30: 125–138
Wan L, Yao B C, Wu N Y. 2000. The extending of Honghe fault in the South China Sea and its tectonic significance (in Chinese). Gresear Eol South China Sea, 12: 22–32
Wang D H, Qu W J, Li Z W, Ying H L, Chen Y C. 2005. Mineralization episode of porphyry copper deposits in the Jinshajiang-Red River mineralization belt: Re-Os dating. Sci China Ser D-Earth Sci, 48: 192–198
Wang Er Q, Fan C, Wang G, Shi X H, Chen L Z, Chen Z L. 2006. Deformational and geomorphic processes in the formation of the Ailaoshan-Diancangshan range west Yunnan (in Chinese). Quat Sci, 26: 220–227
Wang F Y, Pan S Z, Liu L, Liu B F, Zhang J S, Deng X G, Ma C J, Zhang C J. 2014. Wide angle seismic exploration of Yuxi-Lincang profile—The research of the structure of the Red River fault zone and southern Yunnan (in Chinese). Chin J Geophys, 57: 3247–3258
Wang P, Wang L, Mi N, Liu J, Li H, Yu D, Xu M, Wang X, Guo Z. 2010. Crustal thickness and average V_p/V_s ratio variations in southwest Yunnan, China, from teleseismic receiver functions. J Geophys Res, 115: B11308
Wang X, Chen L, Ai Y S, Xu T, Jiang M M, Ling Y, Gao Y F. 2018. Crustal structure and deformation beneath eastern and northeastern Tibet revealed by P-wave receiver functions. Earth Planet Sci Lett, 497: 69–79
Wang Y, Li Q L, Ran H, Zhao C P, Liu Y W. 2018. Geothermal and seismic activities in the southeastern Tibetan Plateau: Constraints from Helium isotopes (in Chinese). Bull Mine Petrol Geochem, 37: 652–662
Ward K M, Lin F, Schmandt B. 2018. High-resolution receiver function imaging across the Cascadia subduction zone using a dense nodal array. Geophys Res Lett, 45: 12218–12225
Wu Z B, Xu T, Wu C L, Zhang M H, Tian X B, Teng J W. 2016. Crustal shear-wave velocity structure beneath the western Tibetan Plateau revealed by receiver function inversions (in Chinese). Chin J Geophys, 59: 516–527
Xu L L, Rondenay S, van H R D. 2007. Structure of the crust beneath the southeastern Tibetan Plateau from teleseismic receiver functions. Phys Earth Planet Inter, 165: 176–193

Xu M, Wang L, Liu J, Zhong K, Li H, Hu D, Xu Z. 2006. Crust and uppermost mantle structure of the Ailaoshan-Red River fault from receiver function analysis. Sci China Ser D-Earth Sci, 49: 1043–1052
Xu Q, Zhao J M. 2008. A review of the receiver function method (in Chinese). Proc Geophys, 23: 1709–1716
Xu T, Zhang Z J, Liu B F, Chen Y, Zhang M H, Tian X B, Xu Y G, Teng J W. 2015. Crustal velocity structure in the Emeishan large igneous province and evidence of the Permian mantle plume activity. Sci China Earth Sci, 58: 1133–1147
Xu X M, Ding Z F, Zhang F X. 2015. The teleseismic tomography study by P-wave travel-time data beneath the southern South-north Seismic Zone (in Chinese). Chin J Geophys, 58: 4041–4051
Xu Y. 2005. Crust and upper mantle structure of the Ailao Shan-Red River fault zone and adjacent regions. Sci China Ser D-Earth Sci, 48: 156–164
Xu Z Q, Yang J S, Li H B, Ji S C, Zhang Z M, Liu Y. 2011. On the tectonics of India-Asia collision (in Chinese). Acta Geol Sin, 85: 1–33
Yuan S S, Ge L S, Lu Y M, Guo X D, Wang M J, Wang Z H, Zou Y L. 2010. Relationship between crust-mantle reaction and gold mineralization in Ailaoshan metallogenic belt: A case study of Daping gold deposit in Yuanyang (in Chinese). Miner Deposit, 29: 253–264
Zhang F X, Wu Q J, Ding Z F. 2018. A P-wave velocity study beneath the eastern region of Tibetan Plateau and its implication for plateau growth (in Chinese). Chin Sci Bull, 63: 1949–1961
Zhang Z, Xu C M, Meng B Z, Liu C, Teng J W. 2007. Crustal reflectivity characters from the Eryuan-Jiangchuan wide-angle seismic profile (in Chinese). Chin J Geophys, 50: 1082–1087
Zheng T Y, Chen L, Zhao L, Xu W, Zhu R. 2006. Crust-mantle structure difference across the gravity gradient zone in North China Craton: Seismic image of the thinned continental crust. Phys Earth Planet Inter, 159: 43–58
Zheng T Y, Zhu R X, Zhao L, Ai Y S. 2012. Intralithospheric mantle structures recorded continental subduction. J Geophys Res, 117: B03308
Zhong D L, Ding L. 1996. Rising process of the Qinghai-Xizang (Tibet) Plateau and its mechanism. Sci China Ser D-Earth Sci, 39: 369–379
Zhu L P, Kanamori H. 2000. Moho depth variation in southern California from teleseismic receiver functions. J Geophys Res, 105: 2969–2980
Zhu X P, Mo X X, Noel C W, Zhang B, Sun M X, Wang S X, Zhao S L, Yang Y. 2009. Geology and metallogenic setting of the Habo porphyry Cu (Mo-Au) deposit, Yunnan (in Chinese). Acta Geol Sin, 83: 1915–1928

(Responsible editor: Huajian YAO)